Supporting Information:

Effects of the Grazing Incidence Geometry on X-Ray Photon Correlation Spectroscopy Measurements

*Christopher R. Greve[a], Meike Kuhn[a], Fabian Eller[a], Michael A. Buchhorn[a], Alexander Hexemer[b], Guillaume Freychet[c,d], Lutz Wiegart[c] and Eva M. Herzig[a]**

[a]Herzig Group – Structure Formation and Dynamics, University of Bayreuth, Universitätsstr. 30, Bayreuth, Bavaria, 95447, Germany

[b]Advanced Light Source, Lawrence Berkeley National Lab, 1 Cyclotron Rd, Berkeley, CA, 94720, USA

[c]National Synchrotron Light Source II, Brookhaven National Laboratory, 98 Rochester St, Upton, New York, 11973, USA

[d]Université Grenoble Alpes, CEA, Leti, 17 Av. des Martyrs, F-38000 Grenoble, France

---

*Corresponding author: Eva M. Herzig (eva.herzig@uni-bayreuth.de, +49(0)981-55-2619)

This file contains:

Section S1: XPCS data extraction

X-ray photon correlation spectroscopy (XPCS) is a scattering technique, which probes the dynamics present in bulk materials as well as at their surfaces and interfaces [1]. The measurement setup is identical to time-resolved small angle x-ray scattering (SAXS) and a series of subsequent scattering images is recorded (Fig. S1a) [2]. In contrast to SAXS, where only minimally coherent x-ray beams are used and where the far-field scattering arises from interference between and within nano objects [3], the use of highly coherent x-ray beams in XPCS produces speckled scattering patterns. The produced speckles arise from scattering due to the structural arrangement of electron density differences within the material present in the illuminated coherence volume [4]. As known from Dynamic Light Scattering (DLS), the time for speckles to decorrelate offers a measure to quantify dynamical properties of the sample in the illuminated coherence volume [5].

For non-equilibrium systems the dynamics can be characterized via the calculation of two-time correlation functions (2TCF) from the measured time-resolved scattering pattern *I(q,t)* at reciprocal scattering vector q and time t [6,7]:

$$C(q, t_1, t_2) = \frac{\langle I(q, t_1) I(q, t_2) \rangle}{\langle I(q, t_1) \rangle \langle I(q, t_2) \rangle}. \quad \text{(S1)}$$

Herein the average $\langle\ \rangle$ is calculated by averaging over a small range of q (in horizontal direction q_r and vertical direction q_z for grazing incidence geometry, see Fig. S2 for Regions of Interest). As visible from Fig. S1b) the maximum of the correlation occurs for $t_1 = t_2$ and will decay as a function of the lag time $\tau = |t_1 - t_2|$ [6]. From the calculated 2TCF steady-state dynamics are obtained for a deterioration time $\bar{t} = \frac{t_1 + t_2}{2}$ by extracting 'aged' one-time intensity autocorrelation functions $g_2(q, \tau)$ (aged-1TCF) [6]:

$$g_2(q,\tau) = \left\langle \frac{\langle I\left(q,\bar{t}-\frac{\tau}{2}\right) I(q,\bar{t}+\frac{\tau}{2})\rangle}{\langle I\left(q,\bar{t}-\frac{\tau}{2}\right)\rangle \langle I(q,\bar{t}+\frac{\tau}{2})\rangle} \right\rangle_{\bar{t}\pm\Delta\bar{t}} . \quad \text{(S2)}$$

To enhance statistics for steady-state dynamics, extracted aged-1TCFs are averaged over a range of deterioration times, where the extracted aged-1TCF are invariant. In the presented data each aged-1TCF is averaged over 20 frames if no avalanche-like behaviour is visible within the 2TCF, corresponding to $\Delta\bar{t}$ = 2 s of administered beam. Furthermore, the aged-1TCF is connected to the intermediate scattering function $g_1(q,\tau)$ (ISF) via the Siegert relation and can therefore be calculated from it. [8]

Figure S1b) exemplifies the principle, which was adopted in this study, to calculate 2TCF from a taken x-ray image series and how the deterioration time $\bar{t}$ and the lag time τ are defined.

To analyze the dynamics in the extracted aged-1TCF an exponential fit of the following form is employed:

$$g_2(\tau) = \beta * \exp(-2(\Gamma\tau)^{\gamma}) + g_\infty. \quad \text{(S3)}$$

In eq. (S3) β is the contrast or Siegert factor, defined by the geometry, sample and the coherence of the incident beam [6], γ is the Kohlrausch-Williams-Watts (KWW) exponent [9] of a stretched exponential, Γ is the characteristic frequency of decay (with $1/\Gamma$ giving the correlation time τ_0) and g_∞ the ergodicity plateau reached for $\tau \to \infty$. Such an approach is well-known for soft matter systems and glass-formers showing diffusive and/or hyper diffusive dynamics [10–13].

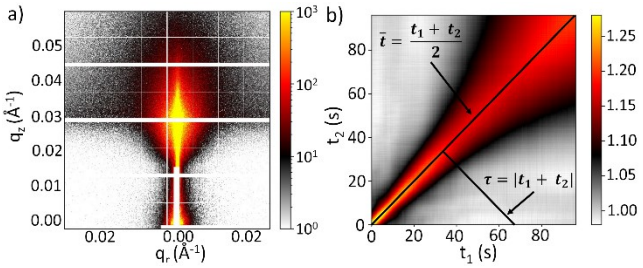

Figure S1. a) GISAXS image obtained from a $MAPbI_3$ thin film, provided by time averaging over 100 frames from a time series around $\bar{t}$ = [50 $\pm$ 10] s. Within the averaged time window, the form of the scattering pattern is not changing. Directions are defined as: q_z as the vertical direction (out-of-plane) and q_r as the horizontal direction (in-plane). b) Two Time Correlation Function (2TCF) calculated for time series of x-ray detector images at (q_z, q_r) = (0.0005 Å^{-1}, 0.0035 Å^{-1}). From the presented 2TCF aged One Time Correlation Functions (aged-1TCF) $g_2(q,\tau)$ are extracted at different deterioration times $\bar{t}$, allowing to analyse how the dynamics inside the system change within a single XPCS measurement. Black diagonal defines $\bar{t}$, the other black line is drawn along a single $g_2(q,\tau)$ curve where the arrow points to a specific τ along the τ-axis and the color in the 2D colormap indicates the magnitude of $g_2(q,\tau)$.

The following figures show the raw data and the ROIs used for analysis within the maintext (Fig S1) and exemplary aged-1TCF of different ROIs (Fig S2 & S3).

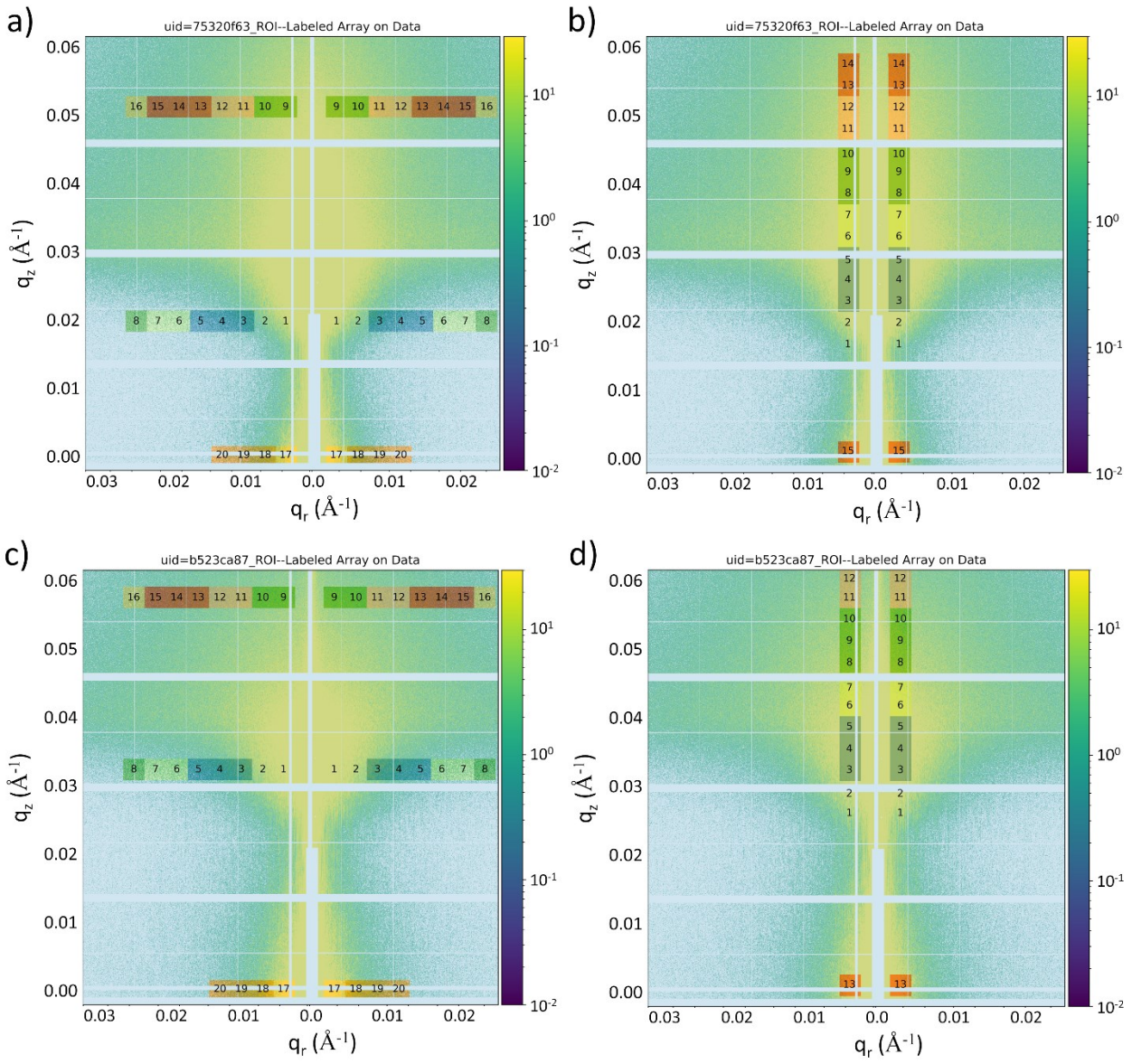

Figure S2. Subgraphs a) & b) show a speckled intensity pattern taken at 0.22° incident angle. Subgraphs a) & b) show a speckled intensity pattern taken at 0.30° incident angle. Subgraph a) & c) shows the Regions of Interest (ROIs) used for calculation of aged-1TCFs in Figure 3 and Figure 4 (main text). Subgraph b) & d) shows the ROIs used for calculation of aged-1TCFs in Figure 2 and Figure 4 (main text).

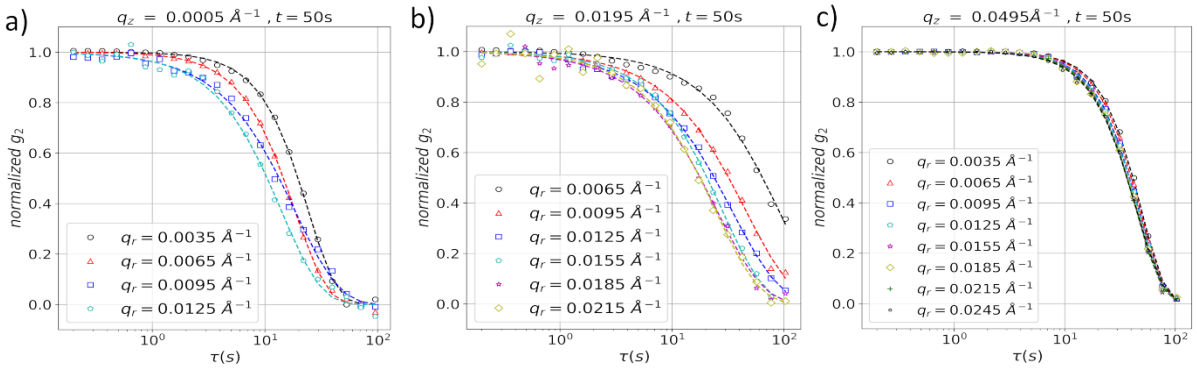

Figure S3. Graph a): Exemplary normalised aged-1TCF on a semi-log time scale extracted at deterioration time $\bar{t}$ = 50 s from 2TCFs calculated from ROIs 17-20 in Figure S2, Subplot a). Graph b): Exemplary normalised aged-1TCF on a semi-log time scale extracted at deterioration time $\bar{t}$ = 50 s from 2TCFs calculated from ROIs 1-8 in Figure S2, Subplot a). Graph c): Exemplary normalised aged-1TCF on a semi-log time scale extracted at deterioration time $\bar{t}$ = 50 s from 2TCFs calculated from ROIs 9-16 in Figure S2, Subplot a). Dotted lines are fits to the aged-1TCFs with a stretched exponential (see eq. S3, section S1).

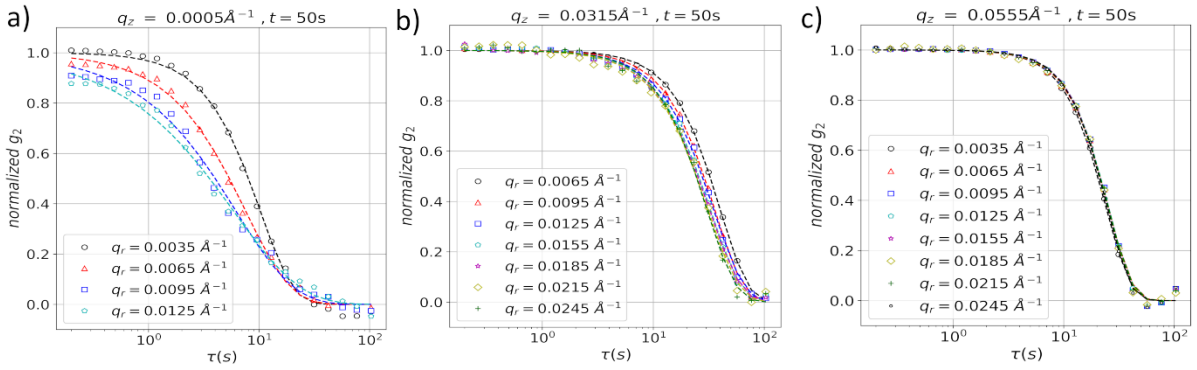

Figure S4. Graph a): Exemplary normalised aged-1TCF on a semi-log time scale extracted at deterioration time $\bar{t}$ = 50 s from 2TCFs calculated from ROIs 17-20 in Figure S2, Subplot c). Graph b): Exemplary normalised aged-1TCF on a semi-log time scale extracted at deterioration time $\bar{t}$ = 50 s from 2TCFs calculated from ROIs 1-8 in Figure S2, Subplot c). Graph c): Exemplary

normalised aged-1TCF on a semi-log time scale extracted at deterioration time $\bar{t}$ = 50 s from 2TCFs calculated from ROIs 9-16 in Figure S2, Subplot c). Dotted lines are fits to the aged-1TCFs with a stretched exponential (see eq. S3, section S1).

Section S2: DWBA introduction

In grazing incidence geometries, the experiments are carried out with small incident angles (θ_i < 1°) to enhance the beam footprint and therefore the effective scattering volume. One distinguishes the grazing incidence transmission (GT) geometry and the grazing incidence (GI) geometry. As visible in Fig. S5 scattering in GT exits below the sample horizon (exit angle $\theta_f < 0°$), thus exiting through the downstream sample edge [14,15], while in GI scattering is detected above the sample horizon ($\theta_f > 0°$). In contrast to scattering in the transmission geometry both GI and GT introduce extra scattering due to reflections taking place within the sample. To describe the reflection related extra scattering the Distorted Wave Born Approximation can be used [16].

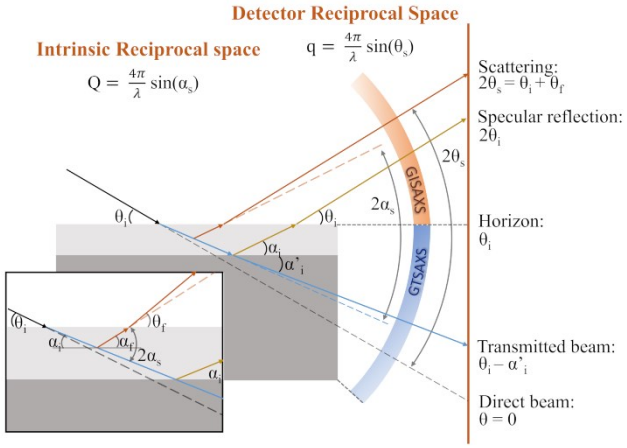

Figure S5. The schematic diagram shows the scattering geometry for grazing incidence experiments. An incident beam (solid black line, incident angle θ_i) is refracted at the air-film and further refracted at the film-substrate interface. The refraction events bend the exiting transmitted beam (blue line) relative to the direct beam. A similar refraction applies to the scattered x-rays (dark orange line) while the beam leaves in the GISAXS region. Also due to refraction the scattering (occurring in the thin film under an angle of $2\alpha_s = \alpha_i + \alpha_f$ in intrinsic sample reciprocal space Q) is projected to the detector at a different scattering angle $2\theta_s = \theta_i + \theta_f$, resulting in an

altered detector reciprocal space q [17]. Adapted with permission from Ref. 17, Copyright 2018, IUCr Journals.

While the DWBA is employed within its simplified form within the main text the DWBA generally describes the intensity on a detector $I_d(q_z)$ along q_z as follows:

$$I_d(q_z) = \left|T(\alpha_i)T(\alpha_f)F(+Q_{z1}) + T(\alpha_i)R(\alpha_f)F(-Q_{z2}) + R(\alpha_i)T(\alpha_f)F(+Q_{z2}) + R(\alpha_i)R(\alpha_f)F(-Q_{z1})\right|^2 \quad \text{(S1)}$$

In equation (S1) the reciprocal vectors Q_{z1} & Q_{z2} consider the beam direction in the film and are thus defined as:

$$Q_{z1} = k(\sin\alpha_i + \sin\alpha_f) \quad \text{(S2a)}$$

$$Q_{z2} = k(\sin\alpha_i - \sin\alpha_f) \quad \text{(S2b)}$$

with $k = 2\pi/\lambda$ and λ the wavelength of the incident x-ray beam. In the utilized definition of reciprocal vectors, Q_{z1} matches the classical definition, while Q_{z2} considers the directional change by a single reflection event. Further, $R(\alpha_i)$ and $R(\alpha_f)$ are the angle dependent Fresnel coefficients of reflectivity for incident angle α_i and exit angle α_f and $T(\alpha_i)$ and $T(\alpha_f)$ are the respective angle dependent Fresnel coefficients of transmissivity. The term *F(Q)* is the scattering strength contribution from the form factor. When expanding equation S1 the formula will result in 16 terms, most of them complex valued. Using the following notation $T(\alpha_i) = T_i$, $R(\alpha_f) = R_f$ and $F(+Q_{z1}) = F_{+1}$, $F(-Q_{z2}) = F_{-2}$ etc the measured intensity on the detector can be written as follows [17] :

$$I_d(q_z) = \left|T_i T_f\right|^2 |F_{+1}|^2 + \left|R_i T_f\right|^2 |F_{+2}|^2 + \left|T_i R_f\right|^2 |F_{-2}|^2 + \left|R_i R_f\right|^2 |F_{-1}|^2$$
$$+ 2\,|T_i|^2 \mathrm{Re}\left[T_f R_f^* F_{+1} F_{-2}^*\right] + 2\left|T_f\right|^2 \mathrm{Re}[T_i R_i^* F_{+1} F_{+2}^*] + 2\,|R_i|^2 \mathrm{Re}\left[T_f R_f^* F_{-1}^* F_{+2}\right]$$
$$+ 2\left|R_f\right|^2 \mathrm{Re}[T_i R_i^* F_{-1}^* F_{-2}] + 2\mathrm{Re}\left[T_i R_i^* T_f R_f^* F_{+1} F_{-1}^*\right]$$
$$+ 2\mathrm{Re}\left[T_i R_i^* T_f^* R_f F_{+2}^* F_{-2}\right]. \quad \text{(S3)}$$

In equation (S3) the first four terms are real and positive valued and can be interpreted as the intensities resulting from the four (independent) scattering terms in the DWBA. The residual terms are cross terms between the first four terms, resulting in interference effects altering the observed scattering pattern by enhancing or diminishing the intensity signal on the detector. In the physical (disperse) system mentioned within the main text, the scattering signal arises from an ensemble of nano formations, giving an average over the ensemble. The ensemble average over these structures results in the proportion of the cross-term signals to be insignificant [18], only giving rise to high-frequency modulations, which can be ignored in the further data analysis [19].

Section S3: Fresnel reflectivity & transmissivity calculations

The calculation of intensities for GISAXS as well as GTSAXS experiments within the DWBA relies on the computation of the reflectivities and transmissivities modulating the measured intensity on the detector. For the calculation the intensity in the transmitted and reflected beams impinging on the sample needs to be addressed (with the scattering being proportional to the arriving photon flux). The following calculations are based on the widely accepted standard method for reflectivity calculations[20]. To calculate the reflectivity for layered systems, we start from the influence on the vertical component of the impinging wave vector of a single interface and how the traverse of the interface alters the named component:

$$k_z = -\sqrt{k_0^2 + |k_{||}|^2}, \text{(S1)}$$

$$k_{z,j} = -\sqrt{n_j^2 k_0^2 + |k_{||}|^2}. \text{(S2)}$$

With $k_0 = 2\pi/\lambda$, $n_j = 1 - \delta - i\beta = \cos(\theta_c)$ the refractive index of the layer and $k_{||} = k_0\cos(\alpha)$ the in-plane component of the impinging wave vector under the incidence angle α. With $k_{z,j}$ the Fresnel coefficients can be written as:

$$r_f = \frac{k_z - k_{z,j}}{k_z + k_{z,j}}, \text{(S3a)} \quad t_f = \frac{2k_z}{k_z + k_{z,j}} . \text{(S3b)}$$

In a generalized form for a multilayer model the coefficients can be modified for an interface between layer j and j+1:

$$r_{j,j+1} = \frac{k_{z,j} - k_{z,j+1}}{k_{z,j} + k_{z,j+1}}, \text{(S4a)} \quad t_{j,j+1} = \frac{2k_{z,j}}{k_{z,j} + k_{z,j+1}} \text{(S4b)}$$

This approach only calculates single reflectivities and transmissivities, not considering the influence of underlying layers of certain thickness and their corresponding reflectivities and

transmissivities. To consider reflections by different interfaces and the resulting interference among themselves the phase offset (determined by the height h_{j+1} of layer j+1) is considered:

$$R_{j,j+1} = \frac{r_{j,j+1} + R_{j+1,j+2}\exp\left(2ih_{j+1}k_{z,j+1}\right)}{1 + r_{j,j+1}R_{j+1,j+2}\exp\left(2ih_{j+1}k_{z,j+1}\right)} \quad \text{(S5a)}$$

$$T_{j,j+1} = \frac{t_{j,j+1}t_{j+1,j+2}\exp\left(ih_{j+1}k_{z,j+1}\right)}{1 + r_{j,j+1}R_{j+1,j+2}\exp\left(2ih_{j+1}k_{z,j+1}\right)} \quad \text{(S5b)}$$

Resulting for a single layer of thickness h in the known equations for r_s and t_s:

$$r_s = \frac{r_{0,1} + r_{1,2}\exp\left(2ihk_{z,1}\right)}{1 + r_{0,1}r_{1,2}\exp\left(2ihk_{z,1}\right)} \quad \text{(S6a)}$$

$$t_s = \frac{t_{0,1}t_{1,2}\exp\left(ihk_{z,1}\right)}{1 + r_{0,1}r_{1,2}\exp\left(2ihk_{z,1}\right)} \quad \text{(S6b)}$$

Like the vertical components k_z. the transmissivities and reflectivities are complex valued, resulting in interference effects when multiplied with each other. But due to the simplification to the DWBA made in the main text (simplified DWBA) only magnitudes of $|R|^2$ and $|T|^2$ are used to calculate simplified DWBA prefactors.

To illustrate the complex character of the Fresnel coefficients an example of reflectivity (r) and transmissivity (t) on a silicon substrate is shown in Fig. S6.

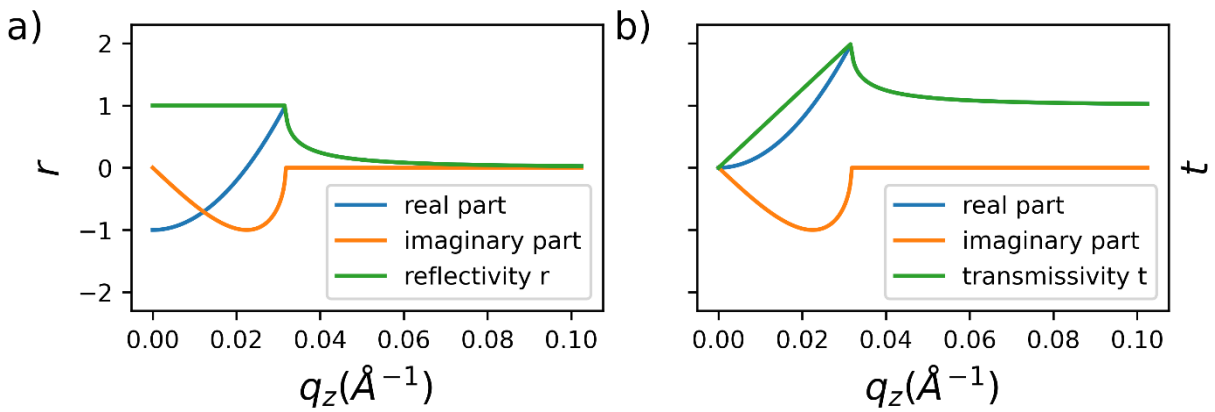

Figure S6. Example on the behaviour of a) the reflectivity (r) and b) transmissivity (t) Fresnel coefficients for a single interface of Silicon, calculated with an x-ray energy of 9.65 keV. For each coefficient the real part, imaginary part and the absolute is shown.

Section S4: Refraction influence to scattering origin in GI & GT

Due to refraction altering detected angles it is necessary to distinguish between the intrinsic thin film reciprocal space Q within the thin film and the measured detector reciprocal space q. The intrinsic reciprocal space Q is defined as:

$$Q = 2k\sin(\alpha_s), \tag{S1}$$

where k and λ follow the earlier definition and α_s is the scattering angle within the thin sample. As shown in Fig. S5 intrinsic scattering is seen under $2\alpha_s$ projected to higher angles on the detector of $2\theta_s$. Thus, intrinsic scattering with Q is projected onto the detector reciprocal space $q = 2k\sin(\theta_s)$. As shown by Lu *et al.* [15] the difference between intrinsic Q and detector q is highly non-linear near the critical angle θ_c of the impinged thin film. Importantly, the refraction affects only the z-direction and (for the small angles used here) will not alter the shift in the scattering signal on the detector along the horizontal q_r-component. To calculate the refraction shift reducing the angle at the atmosphere/thin film interface one can use the following cosine form of Snell's law as a function of the critical angle θ_c of the thin film: $\cos(\alpha_i) = \frac{\cos(\theta_i)}{\cos(\theta_c)}$. Further, refraction needs to be considered when scattered electromagnetic waves travel across the thin film/substrate interface. The second refraction follows the same form of Snell's law but using the critical angle θ_{si} of the substrate.

Hereby Q_z will be calculated using the cosine form of Snell's law for the classical definition of Q_z as discussed above. Two different cases need to be distinguished. The so-called transmission channel (Tc) addresses the scattering contributions containing no or double reflections (valid for $\left|T_i T_f\right|^2 |F_{+1}|^2$ and $\left|R_i R_f\right|^2 |F_{-1}|^2$). In the reflection channel (Rc) (valid for $\left|R_i T_f\right|^2 |F_{+2}|^2$and $\left|T_i R_f\right|^2 |F_{-2}|^2$) we take into account the known shift of the scattering in Rc in relation to Tc, which

is proportional to $2\theta_i$ [21]. The shift can be seen, as an incident angle dependent splitting of Rc and Tc in Figure 1b (main text) that occurs if an odd number of reflections occurs. For GT we need to consider one DWBA term of each channel. We define the intrinsic Q_{zI} from $\left|T_i T_f\right|^2 \ |F_{+1}|^2$ for the transmission channel in GT, which can be written in the following way:

$$Q_{z,GT,Tc} = 2k \sin\left(\frac{\alpha_i - \alpha_f}{2}\right)$$

$$\cong k\left((\sin^2\theta_i - \sin^2\theta_c)^{\frac{1}{2}} - \left(\sin^2\theta_f + \sin^2\theta_{Si} - \sin^2\theta_c\right)^{\frac{1}{2}}\right) \qquad \text{(S2a)}$$

To take into account the above mentioned shift between Rc and Tc of ~$2\theta_i$ [21] in grazing incidence geometries for the reflection channel Rc equation (S2a) needs to include the reflection shift introduced in the definition of Q_{z2} (see section S2, equation (S2b)). This will result in the following intrinsic $Q_{z,GT,Rc}$:

$$Q_{z,GT,Rc} = 2k \sin\left(\frac{-\alpha_f - \alpha_i}{2}\right)$$

$$\cong k\left(\left(\sin^2\theta_f + \sin^2\theta_{Si} - \sin^2\theta_c\right)^{\frac{1}{2}} - (\sin^2\theta_i - \sin^2\theta_c)^{\frac{1}{2}}\right) \qquad \text{(S2b)}$$

Additionally, like for GTSAXS, the non-linear contribution of refraction on the projection of intrinsic Q to the detector q is important to understand the origin of scattered intensity on the detector. As in the GTSAXS section the difference of $\Delta q_z = q_z - Q_z$ is calculated. With $Q_{z,GI,Tc}$ being the intrinsic Q_z for the DWBA terms $\left|T_i T_f\right|^2 \ |F_{+1}|^2$ and $\left|R_i R_f\right|^2 \ |F_{-1}|^2$) in the transmission channel Tc:

$$Q_{z,GI,Tc} \cong k\left[(\sin^2\theta_i - \sin^2\theta_c)^{\frac{1}{2}} + \left(\sin^2\theta_f - \sin^2\theta_c\right)^{\frac{1}{2}}\right]. \qquad \text{(S3a)}$$

In contrast to Eq. (S2a) refraction only occurs at the air-film interface and depends on the materials critical angle θ_c.

To consider the vertical shift in Δq_z for the reflection channel Rc (relevant for scattering related to the DWBA terms $\left|R_i T_f\right|^2 |F_{+2}|^2$and $\left|T_i R_f\right|^2 |F_{-2}|^2$) equation (S3a) needs to be extended to include the effect of an angular offset arising from an odd number of reflections analogous to GTSAXS. This will result in the following intrinsic $Q_{z,GI,Rc}$:

$$Q_{z,GI,Rc} \cong k\left[\left(\sin^2\theta_f - \sin^2\theta_c\right)^{\frac{1}{2}} - \left(\sin^2\theta_i - \sin^2\theta_c\right)^{\frac{1}{2}}\right]. \quad \text{(S3b)}$$

To describe the refraction effect on the difference introduced in the main text of $\Delta q_z = q_z - Q_z$ the intrinsic reciprocal space vector must be written in terms of incident θ_i and scattering angles θ_f, resulting in 4 different terms for the reflection channel Rc, transmission channel Tc and GI and GT geometry [15].

The classical definition of the refraction shift in the transmission channel for GI geometry can be written as follows:

$$\begin{aligned}
&\Delta q_{z,Tc,GI} = q_z - Q_z \\
&= q_z - 2k\sin(\alpha_s) \\
&= q_z - 2k\sin\left(\frac{\alpha_i + \alpha_f}{2}\right) \\
&= q_z - 2k\sin\left(\frac{1}{2}\arccos\left(\frac{\cos\theta_i}{\cos\theta_c}\right) + \frac{1}{2}\arccos\left(\frac{\cos\theta_f}{\cos\theta_c}\right)\right) \\
&\cong q_z - k\left(\left(\sin^2\theta_i - \sin^2\theta_c\right)^{\frac{1}{2}} + \left(\sin^2\theta_f - \sin^2\theta_c\right)^{\frac{1}{2}}\right) \quad \text{(S4a)}
\end{aligned}$$

To include refraction effects by the substrate for scattering in GT geometry one must include a second refraction event (silicon interface, critical angle θ_{Si}) as well as the change of the direction of the scattering angle:

$$\Delta q_{z,Tc,GT} = q_z - Q_z$$

$$= q_z - 2k \sin\left(\frac{\alpha_i - \alpha_f}{2}\right)$$

$$\cong q_z - k\left((\sin^2\theta_i - \sin^2\theta_c)^{\frac{1}{2}} - \left(\sin^2\theta_f + \sin^2\theta_{Si} - \sin^2\theta_c\right)^{\frac{1}{2}}\right) \quad \text{(S4b)}$$

To include the directional change for the reflection channel leading to the known shift in scattering $\sim 2\theta_i$ [21] the reflection channel shift in GI geometry can be written as follows:

$$\Delta q_{z,Rc,GI} = q_z - 2k \sin\left(\frac{\alpha_f - \alpha_i}{2}\right)$$

$$= q_z - 2k \sin\left(\frac{1}{2}\arccos\left(\frac{\cos\theta_f}{\cos\theta_c}\right) - \frac{1}{2}\arccos\left(\frac{\cos\theta_i}{\cos\theta_c}\right)\right)$$

$$\cong q_z - k\left(\left(\sin^2\theta_f - \sin^2\theta_c\right)^{\frac{1}{2}} - (\sin^2\theta_i - \sin^2\theta_c)^{\frac{1}{2}}\right) \quad \text{(S4c)}$$

Going for the reflection channel to the GT region includes again the refraction event at the substrate as well as the directional change in scattering angle, leading to:

$$\Delta q_{z,Rc,GT} = q_z - 2k \sin\left(\frac{-\alpha_f - \alpha_i}{2}\right)$$

$$= q_z - 2k \sin\left(-\frac{1}{2}\arccos\left(\frac{\cos\theta_f}{\cos\theta_c}\right) - \frac{1}{2}\arccos\left(\frac{\cos\theta_i}{\cos\theta_c}\right)\right)$$

$$\cong q_z - k\left(\left(\sin^2\theta_f + \sin^2\theta_{Si} - \sin^2\theta_c\right)^{\frac{1}{2}} - (\sin^2\theta_i - \sin^2\theta_c)^{\frac{1}{2}}\right) \quad \text{(S4d)}$$

The result of Δq_z vs q_z is seen in Fig. 1b (maintext). The GISAXS region is located at q_z higher than the undefined q_z region, explained in the GTSAXS section. It is visible in Fig. 1b (maintext) that exit angles near the materials critical angle result in non-linear behaviour between detector q_z and intrinsic Q_z, while at higher exit angles Δq_z approaches a constant value.

Further, with this framework in place, we can further calculate how Q_z is projected on the detector along q_z in the GI region. This is especially useful, due to the behaviour of Q_z in the Rc, resulting in a decrease of the absolute projected $|Q_z|$ between the Yoneda-region and the specular beam position. The results are shown in Fig S7.

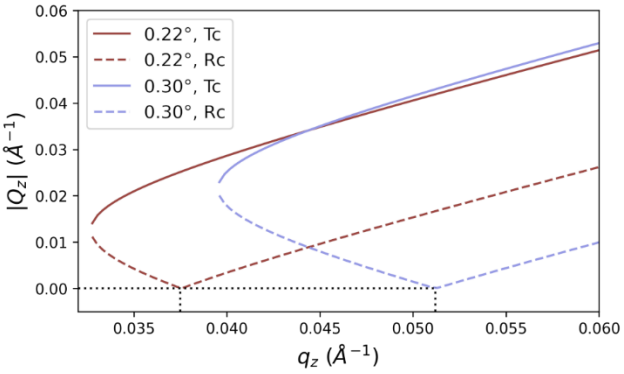

Figure S7. The figure shows a plot of the absolute $|Q_z|$ against q_z for the Tc (full lines) and Rc (dashed lines) within the GI region above the respective Yoneda positions for incident angles of θ_i = 0.22° (brown lines) and θ_i = 0.30° (blue lines). The black dotted vertical lines mark the reversal point of decrease in absolute $|Q_z|$ to increase in absolute $|Q_z|$, which coincidences with the respective specular q_z positions for the calculated incident angles θ_i.

Section S5: Considerations on setup parameters and q-range for coherent scattering experiments

When choosing the parameters for an XPCS experiment some aspects must be considered. Operation at energies E far away from any absorption edges of the used materials are desirable. Further, the contrast β, which is influenced by the ratio of speckle size σ and the pixel size p of the used detector should be maximized. The speckle size can be approximated as follows[22]:

$$\sigma = \frac{\lambda d}{a} \quad \text{(S1)}$$

Hereby λ is the wavelength of the used x-ray radiation, d the sample detector distance (SDD) and a the size of the used x-ray source. In the best case scenario,$\sigma \approx p$ can be achieved (Falus et al. 2006). If several speckles are projected to a single pixel ($\sigma < p$) the contrast will be reduced, and data quality is decreased. In the reversed case ($\sigma > p$) one speckle is detected on several pixels. This can lead to smearing of signal but will not decrease the data quality as harshly as if several speckles are detected within one detector pixel [23].

In the present study we used an Eiger 4M with a pixel size d of 75 µm, placed 13 m downstream of the sample with a beam size (FWHM) of 10 µm. This results in a speckle size of 167 µm. This could have been minimized with an effective SDD of 7 m to the best-case scenario of $\sigma \approx p$. But to achieve a finer q resolution in the GT region a longer SDD was chosen. This was necessary to get the maximum out of the strongly attenuated scattering in the GT region.

With the setup parameters fixed the accessible q-range is then given by the maximum exit angle, which is dependent on the chosen SDD and detector size. With an SDD of 13 m and a detector size of 15.51 cm (2068 pixel) this relates to a maximum exit angle of 0.68°. If the direct beam

position at q_z = 0 is chosen to be on the detector the q_z range can be calculated following the formula for the detector reciprocal space given in Fig. S5.

Section S6: Q-mixing due to setup geometry and ROI

When relating in this study to q-mixing mainly the impact of reflection and refraction is discussed, but several other setup parameters and the approach of analysis can lead to q-mixing, which can influence the aged-1TCF shape. These cases are shortly addressed here to demonstrate that the impact of these is several times or several orders of magnitude smaller than the effect introduced by reflection and refraction near to the materials substrate critical angle.

The simplest case is the effect from the finite size of a single detector pixel. Hereby a certain q-range is projected together into one pixel. As seen from Fig. S8a the effect introduced is constant with the detector within the small angle range and in contrast to Δq_z from Fig. 1b (maintext) up to 3 orders of magnitude smaller.

Another setup related case is the influence of the change in SDD by the finite size of the sample (here: 1 cm maximum footprint or smaller and 13 m for SDD) and/or the elongated footprint. The change in SDD leads to different q_z values projected within the same detector pixel. The difference is dependent on the exit angle and related to the change in SDD. As visible in Fig. S8b the shift by changed SDD in this study is in most of the used q_z-range smaller than the effect from mixing of q_z within a single pixel. For calculation a SDD of 13 m and a change of 1 cm, related to the sample size was used.

A bigger impact is related to the finite size of the ROIs used for analysis. In the present study we used quadratic ROIs with a length of 0.003 $Å^{-1}$, introducing q-mixing of the same order on the detector (see Figure S8c). Compared to the difference between Rc and Tc seen in Fig. 1b (maintext) this can still be seen as negligible, but can add up if bigger ROIs are chosen, especially if the ROIs are in the highly non-linear region related to the materials critical angle. The effect can be limited by choosing smaller ROIs in q_z, but hereby the usable photon counts are directly proportional to the ROI size used to calculate aged-1TCFs. This can limit the reliability of aged-1TCF, which

bigger ROIs along q_r can adjust for, but introducing again a lower resolution along the horizontal direction.

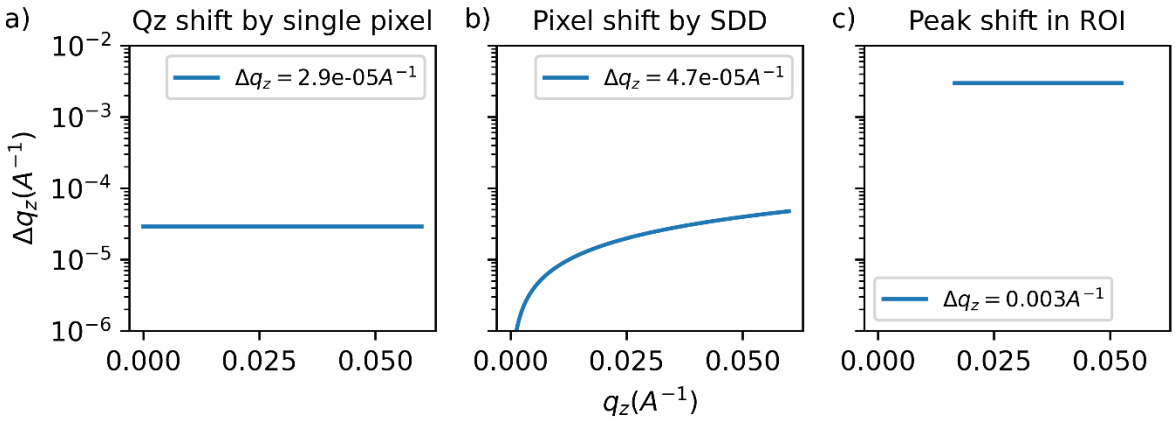

Figure S8. The figure shows a comparison for q-mixing as the shift given by $\Delta q_z = q_{z1} - q_{z2}$ (two positions on the detector) for different cases for a fixed incident angle of 0.30°. Graph a) shows the difference Δq_z vs q_z introduced by single pixel size (Eiger 4M). Graph b) shows the behaviour of Δq_z vs q_z from the change of SDD at 13 m given by the elongated footprint on a finite sample (1cm) in GI-geometry projected to an Eiger 4M. Graph c) shows the difference Δq_z vs q_z given by finite ROI size necessary to conduct the experiments of the study with sufficient photon statistics.

Section S7: Calculations on Homo- and Heterodyning

Another important aspect to consider when analysing XPCS data is the occurrence of homodyne and heterodyne mixing, in the chosen measurement geometry. From C. Gutt et al. [24] it is known, that dependent on the applicable limit to describe scattering events (Fraunhofer or Fresnel limit) the distance between aperture and sample will lead to overlap of Fourier components when these are within the broadening due to the aperture function. Due to this specularly reflected or directly transmitted x-rays can overlap with diffusely scattered x-rays. The reciprocal length scale in the Fresnel limit up to which homo- and heterodyne mixing occurs is given by $k^2 s$, with $k^2 = \frac{2\pi}{\lambda L_a}$ (λ: wavelength, L_a: aperture − sample distance) and s being a measure of the aperture size. In our given measurement geometry with an approximated aperture size of 10 µm and an aperture-sample distance of 1 m this would lead to an upper limit of q-space of 0.0005 Å^{-1}. So, one would expect around 0.0005 Å^{-1} around the direct beam position and the specular beam position to detect a mixed hetero and homodyne detection scheme. With a start q_r of 0.0035 Å^{-1} of the used ROI series, we don't expect mixed detection scheme to be present in our chosen Regions of Interest.

Further Skihaluridze et al.[25] showed that one would expect a jump in contrast when moving from one detection scheme to the other. This is related to the nature of heterodyne mixing, which is modulated with a strong elastic signal (direct or reflected beam), while in homodyne mixing the signal is modulated with itself, a weaker quasi-elastic signal. To demonstrate that no sharp jumps in contrast occur the contrast factors β of the data points presented in Figure 5 are shown in Fig. S9.

Based on this we conclude that homo- and heterodyne mixing is not present within our chosen regions of interest for data analysis and that we operate only within a homodyne detection scheme, far enough away from specular reflected x-rays and/or the direct beam.

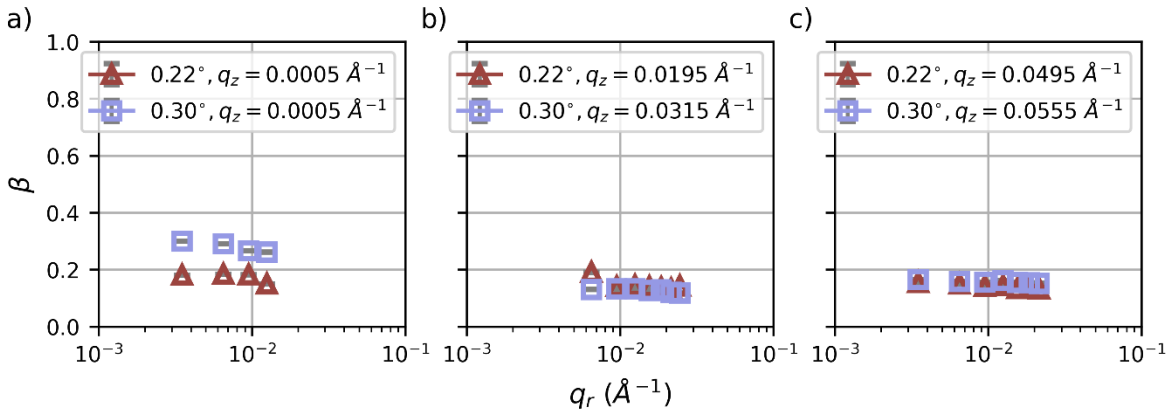

Figure S9. The figure shows the contrast factor β vs q_r for the data points shown in Fig. 3 of the main text. Graph a) shows the contrast factor for data points extracted in GT (extracted near q_z = 0), while b) shows surface and c) bulk sensitive q_z regions for GI data (for comparison reasons located below and above the respective Yoneda regions).

Section S8: Calculations on wave vector spread

C. Gutt et al.[26] showed that the resolution parameter Δ representing the wave vector spread $\delta q/q$ can have substantial influence on a detected signal by diminishing the contrast with increasing wave vector spread and/or introducing shifts in the detection scheme. Depending on the system such detection scheme shift is not necessarily obvious. Gutt et al. showed that for a system of overdamped capillary waves, e.g. on a polymer film the shift induces a decrease in extracted relaxation times. Such a decrease could be easily misinterpreted as a change of the present dynamics in such a system. Further, the wave vector spread is depending on the incidence angle α_i and exit angle α_f due to the projection of coherence length and the projection of the beam size. Combining this with various measured q-values on a 2D detector it is necessary to discuss if those detection scheme shifts are expected within our presented manuscript.

Gutt et al. showed that the wave vector spread can be calculated as follows:

$$\delta q_z = 2\pi \sqrt{\frac{2}{\Xi_z^2} + \frac{1}{\Sigma_z^2}\left[1 + \left(\frac{k_0 \Delta a^2}{L_a}\right)^2 \left(1 - \frac{\Sigma_z^2}{\Delta a^2} \frac{L_a sin^2(\alpha_f) + L_b sin^2(\alpha_i)}{L_b}\right)^2\right]} \quad \text{(S1)}$$

$$\delta q_r = 2\pi \sqrt{\frac{2}{\Xi_r^2} + \frac{1}{\Sigma_r^2}\left[1 + \left(\frac{k_0 \Delta a^2}{L_a}\right)^2 \left(1 - \frac{\Sigma_r^2}{\Delta a^2} \frac{L_a + L_b}{L_b}\right)^2\right]} \quad \text{(S2)}$$

With δq_z being the wave vector spread along the beam, δq_r perpendicular to the beam, Ξ being the projected transversal coherence length, Σ being the projected beam size and Δa a measure of the incident aperture size. Further is L_a the aperture-sample distance, L_b the sample-detector distance, $k_0 = 2\pi/\lambda$ the wave number of the incident wavelength. The non-projected coherence length was calculated as $\Xi = \frac{\lambda L_a}{2D}$ with an aperture-sample distance of 1m, a wavelength λ of 1.285 Å and source size D of 10 µm. Further, the following values were used within the calculations: $\Delta a = 10$ µm, $L_b = 13$ m, non-projected beam size $\Sigma = 10$ µm. While for α_i incidence angles of

0.22° and 0.30° were considered. The exit angle α_f ranges between 0.0° and 0.68°, taken from the observable angle range at 13 m sample-detector distance for an Eiger X 4M.

A plot of $\delta q_z/q_z$ is shown in Fig. S10, showing that within our experiments no ratio above 0.01 is expected for q_z. Further we calculated $\delta q_r/q_r$ with the smallest q_r used within the manuscript, which results in a $\delta q_r/q_r$ (q_r = 0.0035 Å^{-1}) ≈ 0.0395. We see that the wave vector spread along q_r will dominate the resolution parameter Δ. With the approximation of Gutt et al. that changes of the detection scheme above 0.2 come into play we conclude that no such changes are expected for our taken experiments.

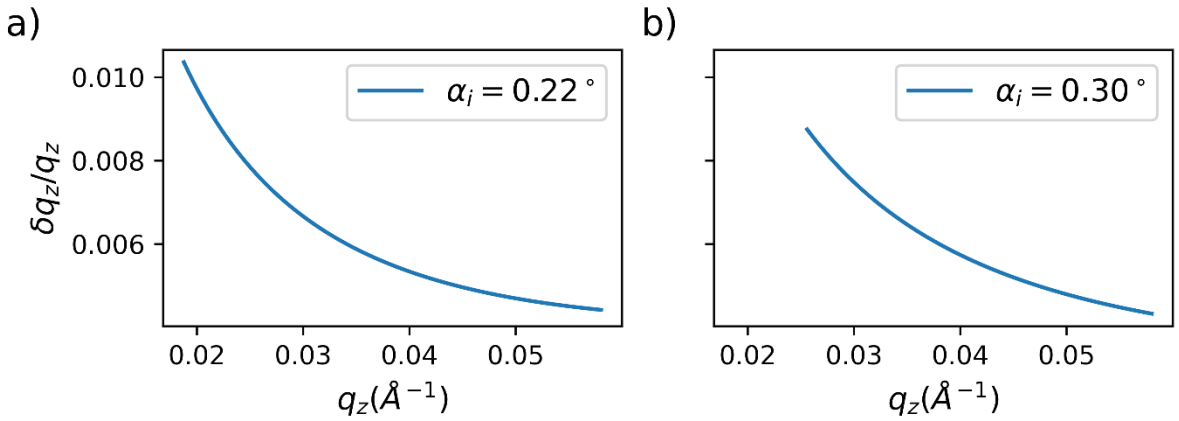

Figure S10. The figure shows the influence of the incidence angle to the wave vector spread $\delta q_z/q_z$. Graph a) shows $\delta q_z/q_z$ vs q_z starting from the q_z value of the horizon for an incidence angle of α_i = 0.22°. Graph b) shows $\delta q_z/q_z$ vs q_z starting from the q_z value of the horizon for an incidence angle of α_i = 0.30°. Both graphs end at a q_z of 0.059 Å^{-1} marking the upper limit of the detector used within the experiments shown within the maintext. For the calculation of $\delta q_z/q_z$ see S8.

Section S9: Generalization of incident angle approximation by Fresnel coefficients

To examine whether a general rule of thumb for BA-term domination can be provided we calculated the Fresnel coefficient representation shown in Fig. 1a (main text) for Methylammonium Lead Iodide ($MAPbI_3$) with layer thicknesses of 800 nm and 20 nm and Poly(3-hexylthiophene-2,5-diyl) (P3HT) with layer thicknesses of 200 nm and 20 nm. Two different energies were used in the calculations: 9.65 keV (identical to the experiments within the study) and 13.5 keV. The critical angle of a thin film is a function of the material and the x-ray energy used, hence to compare incident angles, the applied angle of incidence is expressed as a multiple of the energy dependent material critical angle. The used critical angles were: θ_c(MAPI, 9.65 keV) = 0.163°, θ_c(MAPI, 13.50 keV) = 0.135°, θ_c(P3HT, 9.65 keV) = 0.132°, θ_c(P3HT, 13.50 keV) = 0.095°. The results are shown in Fig 5 (main text) and Fig S11.

From the 2D maps we can see that the material composition has a high impact on the dominant Fresnel coefficients as a function of angle of incidence. For example, for both $MAPbI_3$ thicknesses in Fig 5 a) and b) the BA scattering term is already dominant for $\theta_i = 1.5\ \theta_c$, whereas for P3HT in Fig 5c) and d) a higher incident angle of two times the material critical angle is necessary to reach BA dominated scattering. Further, when comparing Fig 5 and Fig S11 the impact of the x-ray energy has different effects. On the one hand for the higher electron density sample of $MAPbI_3$ (800 nm thick) the prefactor fractions with T_i contributions dominate already at lower θ_i for all q_z (Fig 5a) & Fig S11a)), while we do not observe this behaviour for P3HT where more terms are still relevant at intermediate θ_i. The change of thickness mainly plays a role for the prefactor fractions around the Yoneda region but does not significantly influence for which q_z the BA term dominates. The lowest q_z where the BA term dominates, increases more strongly to higher q_z for the material with the higher electron density while for the lower electron density material the shift is not discernible. In contrast, the q_z, for which the BA dominates the scattering, is not strongly

affected by the change in x-ray energy for the lower density material. For the examples shown using two times the material critical angle as incident angle and double the q_z value of the horizon is a good indicator for obtaining BA dominated data. However, since material and x-ray energy relationships are complex, we recommend to carry out the actual calculations for confirming the ideal measurement conditions for a particular material system and beamline settings.

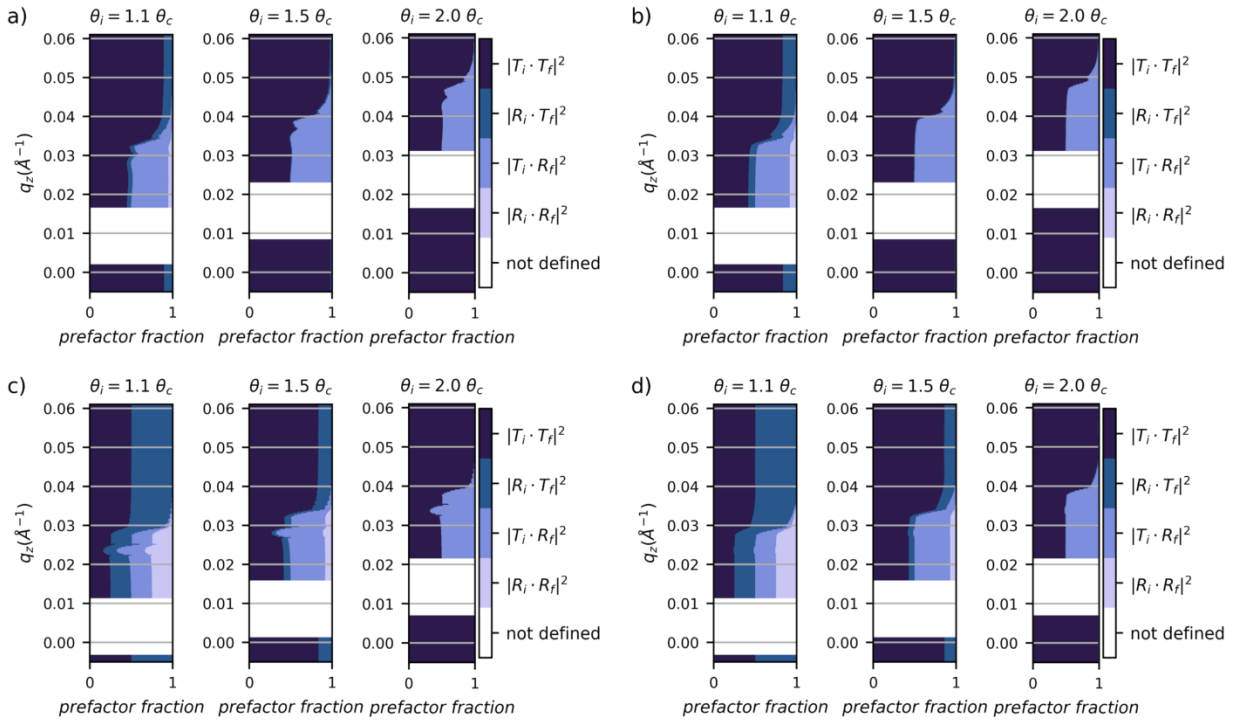

Figure S11. Material dependent Fresnel coefficient analysis used for intensity calculations in the simplified DWBA for incident angles θ_i = 1.1 θ_c, 1.5 θ_c and 2.0 θ_c versus q_z. The reflectivities and transmissivities are calculated for a two-slab system of a) 800 nm thick $MAPbI_3$ b) 20 nm thick $MAPbI_3$ c) 200 nm thick P3HT d) 20 nm thick P3HT placed on a silicon substrate with varying exit angles θ_f which is converted to q_z. Calculations are for an x-ray energy of 13.50 keV (λ = 0.918 Å).

References:

(1) Sinha, S. K.; Jiang, Z.; Lurio, L. B. X-Ray Photon Correlation Spectroscopy Studies of Surfaces and Thin Films. *Adv. Mater.* **2014**, *26*, 7764–7785.

(2) Sutton, M. A Review of X-Ray Intensity Fluctuation Spectroscopy. *C. R. Phys.* **2008**, *9*, 657–667.

(3) Higgins, J.; Stein, R. Recent Developments in Polymer Applications of Small-Angle Neutron, X-Ray and Light-Scattering. *J. Appl. Crystallogr.* **1978**, *11*, 346–375.

(4) Sutton, M.; Mochrie, S.; Greytak, T.; Nagler, S.; Berman, L.; Held, G.; Stephenson, G. Observation of Speckle by Diffraction with Coherent X-Rays. *Nature* **1991**, *352*, 608–610.

(5) Pusey, P.; Van Megen, W. Dynamic Light-Scattering by Non-Ergodic Media. *Physica A* **1989**, *157*, 705–741.

(6) Madsen, A.; Leheny, R. L.; Guo, H.; Sprung, M.; Czakkel, O. Beyond Simple Exponential Correlation Functions and Equilibrium Dynamics in X-Ray Photon Correlation Spectroscopy. *New J. Phys.* **2010**, *12*, 055001.

(7) Malik, A.; Sandy, A.; Lurio, L.; Stephenson, G.; Mochrie, S.; McNulty, I.; Sutton, M. Coherent X-Ray Study of Fluctuations during Domain Coarsening. *Phys. Rev. Lett.* **1998**, *81*, 5832–5835.

(8) Pusey, P. N. D. L. S. *Neutron, X-Rays and Light. Scattering Methods Applied to Soft Condensed Matter*; Th. Zemb, P. Lindner, Ed.; Elsevier North Holland: Amsterdam, 2002; pp. 203–220.

(9) Williams, G.; Watts, D. Non-Symmetrical Dielectric Relaxation Behaviour Arising from a Simple Empirical Decay Function. *Trans. Faraday Soc.* **1970**, *66*, 80+.

(10) Conrad, H.; Lehmkühler, F.; Fischer, B.; Westermeier, F.; Schroer, M.; Chushkin, Y.; Gutt, C.; Sprung, M.; Grübel, G. Correlated Heterogeneous Dynamics in Glass-Forming Polymers. *Phys. Rev. E* **2015**, *91*, 042309.

(11) Orsi, D.; Guzman, E.; Liggieri, L.; Ravera, F.; Ruta, B.; Chushkin, Y.; Rimoldi, T.; Cristofolini, L. 2D Dynamical Arrest Transition in a Mixed Nanoparticle-Phospholipid Layer Studied in Real and Momentum Spaces. *Sci. Rep.* **2015**, *5*, 17930.

(12) Amadei, F.; Thoma, J.; Czajor, J.; Kimmle, E.; Yamamoto, A.; Abuillan, W.; Konovalov, V. O.; Chushkin, Y.; Tanaka, M. Ion-Mediated Cross-Linking of Biopolymers Confined at Liquid/Liquid Interfaces Probed by In Situ High-Energy Grazing Incidence X-Ray Photon Correlation Spectroscopy. *J. Phys. Chem. B* **2020**, *124*, 8937–8942.

(13) Perakis, F.; Gutt, C. Towards Molecular Movies with X-Ray Photon Correlation Spectroscopy. *Phys. Chem. Chem. Phys.* **2020**, *22*, 19443–19453.

(14) Vinogradov, N. A.; Harlow, G. S.; Carla, F.; Evertsson, J.; Rullik, L.; Linpe, W.; Felici, R.; Lundgren, E. Observation of Pore Growth and Self-Organization in Anodic Alumina by Time-Resolved X-Ray Scattering. *ACS Appl. Nano Mater.* **2018**, *1*, 1265+.

(15) Lu, X.; Yager, K. G.; Johnston, D.; Black, C. T.; Ocko, B. M. Grazing-Incidence Transmission X-Ray Scattering: Surface Scattering in the Born Approximation. *J. Appl. Crystallogr.* **2013**, *46*, 165–172.

(16) Sinha, S.; Sirota, E.; Garoff, S.; Stanley, H. X-Ray and Neutron-Scattering from Rough Surfaces. *Phys. Rev. B* **1988**, *38*, 2297–2311.

(17) Liu, J.; Yager, K. G. Unwarping GISAXS Data. *IUCrJ* **2018**, *5*, 737–752.

(18) Lee, B.; Park, I.; Yoon, J.; Park, S.; Kim, J.; Kim, K.; Chang, T.; Ree, M. Structural Analysis of Block Copolymer Thin Films with Grazing Incidence Small-Angle X-Ray Scattering. *Macromolecules* **2005**, *38*, 4311–4323.

(19) Omote, K.; Ito, Y.; Kawamura, S. Small Angle X-Ray Scattering for Measuring Pore-Size Distributions in Porous Low-Kappa Films. *Appl. Phys. Lett.* **2003**, *82*, 544–546.

(20) Renaud, G.; Lazzari, R.; Leroy, F. Probing Surface and Interface Morphology with Grazing Incidence Small Angle X-Ray Scattering. *Surf. Sci. Rep.* **2009**, *64*, 255–380.

(21) Resel, R.; Bainschab, M.; Pichler, A.; Dingemans, T.; Simbrunner, C.; Stangl, J.; Salzmann, I. Multiple Scattering in Grazing-Incidence X-Ray Diffraction: Impact on Lattice-Constant Determination in Thin Films. *J. Synchrotron Radiat.* **2016**, *23*, 729–734.

(22) Hoshino, T.; Kikuchi, M.; Murakami, D.; Harada, Y.; Mitamura, K.; Ito, K.; Tanaka, Y.; Sasaki, S.; Takata, M.; Jinnai, H.; Takahara, A. X-Ray Photon Correlation Spectroscopy Using a Fast Pixel Array Detector with a Grid Mask Resolution Enhancer. *J. Synchrotron Radiat.* **2012**, *19*, 988–993.

(23) Falus, P.; Lurio, L. B.; Mochrie, S. G. J. Optimizing the Signal-to-Noise Ratio for X-Ray Photon Correlation Spectroscopy. *J. Synchrotron Radiat.* **2006**, *13*, 253–259.

(24) Gutt, C.; Ghaderi, T.; Chamard, V.; Madsen, A.; Seydel, T.; Tolan, M.; Sprung, M.; Grubel, G.; Sinha, S. Observation of Heterodyne Mixing in Surface X-Ray Photon Correlation Spectroscopy Experiments. *Phys. Rev. Lett.* **2003**, *91*, 076104.

(25) Sikharulidze, I.; Dolbnya, I.; Madsen, A.; de Jeu, W. X-Ray Photon Correlation Spectroscopy in a Reflection Geometry: Coherence and Resolution. *Opt. Commun.* **2005**, *247*, 111–124.

(26) Gutt, C.; Ghaderi, T.; Tolan, M.; Sinha, S. K.; Gruebel, G. Effects of Partial Coherence on Correlation Functions Measured by X-Ray Photon Correlation Spectroscopy. *Phys. Rev. B* **2008**, *77*, 094133.